



Cite this: *Phys. Chem. Chem. Phys.*,  
2015, 17, 31670

## A new look at oxide formation at the copper/electrolyte interface by *in situ* spectroscopies†

Cigdem Toparli, Adnan Sarfraz and Andreas Erbe\*

The widely used engineering material copper is a prototype of an electrochemically passive metal. In this work, the passive films on evaporated copper in 0.1 M NaOH are investigated *in situ* and *operando* by spectroscopic ellipsometry and Raman spectroscopy, both conducted during oxidation in potentiostatic step experiments. Oxide growth is initiated by jumping from a potential at which the surface is oxide-free to  $-0.1$  V vs. Ag|AgCl|3 M KCl ( $+0.11$  V vs. standard hydrogen electrode, SHE). At subsequent electrode potential jumps, no corresponding jumps in the thickness are observed; instead, oxide growth proceeds steadily. Above  $+0.3$  V vs. Ag|AgCl|3 M KCl ( $+0.51$  V vs. SHE), the oxide layer thickness remains constant at  $\approx 7$  nm. Raman spectra show a peak at  $530\text{ cm}^{-1}$ , which agrees with the dominant peak in spectra of copper mixed oxide,  $\text{Cu}_4\text{O}_3$  ( $\text{Cu}_2^{+}\text{Cu}_2^{II}\text{O}_3$ ). Crystalline  $\text{Cu}_4\text{O}_3$  nucleates from a precursor state showing strong photoluminescence (PL), which hints at the involvement of  $\text{Cu}_2\text{O}$ . Overall, the PL spectra of the growing oxide and absorption spectra indicate the presence of  $\text{Cu}_2\text{O}$  in the thin films. Absorption spectra cannot be understood as a superposition of the spectra from different well-described copper oxides, which points to defect-rich oxides that show rather different spectra. Raman spectra also point to an involvement of both crystalline and amorphous oxides that coexist. The results show that the passive layers on copper are more complex than the duplex layers described in the literature; they do contain an oxide with a mixed valency of copper.

Received 29th August 2015,  
Accepted 2nd November 2015

DOI: 10.1039/c5cp05172j

[www.rsc.org/pccp](http://www.rsc.org/pccp)

## 1 Introduction

Copper is one of the widest used metals because of its availability and good corrosion resistance. As examples, copper canisters are used for nuclear waste disposal, and it is used as an interconnect material for microelectronic devices, as electrical wires, heat exchangers, machine tools and in construction engineering. Thus, understanding the corrosion and passivation of copper is important to ensure a long lifetime of the manufactured devices.<sup>1,2</sup> Copper oxide based corrosion products naturally form on metallic copper, and lead to the passivation of the metal.<sup>3</sup> The term “passivation” is used here to describe a situation in which fast dissolution of a material is expected, but not observed.<sup>4</sup> From a variety of post-mortem studies of oxide growth at high temperatures in different atmospheres, oxide formation is found to start with the formation of  $\text{Cu}_2\text{O}$ .<sup>3,5,6</sup> An outer layer of  $\text{CuO}$  is finally formed, leading to duplex corrosion product layers.<sup>3,7,8</sup> In aqueous solutions, the formation of protective layers is well-described

by the Pourbaix diagram of copper.<sup>9</sup> Different copper oxides can be obtained depending on the applied potential, exposure time and pH. In this context, understanding the corrosion process requires knowledge about the structure, including the electronic structure of the forming films.

Copper oxides received considerable interest for multiple applications, such as spintronic devices, optoelectronics, photocatalysis and solar technology.<sup>10–13</sup> One reason for their popularity is their low band gap, ranging between 2.1 eV for  $\text{Cu}_2\text{O}$  and 1.4 eV for  $\text{CuO}$ .<sup>12,14–20</sup> The two main oxide phases are  $\text{Cu}_2\text{O}$  and  $\text{CuO}$ , the former is considered as one of the most important p-type semiconductors.<sup>21–23</sup> Recently,  $\text{Cu}_2\text{O}$  gained significant interest for solar cells because of its availability and nontoxicity. Consequently also optical and electronic properties of the other oxides,  $\text{CuO}$  and  $\text{Cu}_4\text{O}_3$ , are being investigated for possible applications.<sup>19</sup> Several computational studies were devoted to the analysis of the electronic properties of bulk and thin film  $\text{Cu}_2\text{O}$ .<sup>24,25</sup> However, there appears to be a lack of reliable band-structure calculations for  $\text{CuO}$  and  $\text{Cu}_4\text{O}_3$ . Moreover, the oxide film formed as a corrosion product on metal may have different electronic properties than the bulk oxide.

The formation of copper oxides in solution has been examined e.g. by *in situ* electrochemical atomic force microscopy (ECAFM),<sup>26</sup> *in situ* scanning tunneling microscopy (STM),<sup>27–32</sup> and *in situ* Raman spectroscopy.<sup>33,34</sup> The formation of a partially ordered

Max-Planck-Institut für Eisenforschung GmbH, Max-Planck-Str. 1,  
40237 Düsseldorf, Germany. E-mail: [a.erbe@mpie.de](mailto:a.erbe@mpie.de), [aerbe@arcor.de](mailto:aerbe@arcor.de);  
Fax: +49 211 6792 218; Tel: +49 211 6792 890

† Electronic supplementary information (ESI) available: Time evolution of Raman spectra at different electrode potentials. See DOI: 10.1039/c5cp05172j

OH layer was found at a potential of  $-0.81$  V vs. SHE, while the formation of crystalline Cu<sub>2</sub>O was found at  $-0.11$  V vs. SHE by electrochemical STM.<sup>27</sup> Epitaxial growth of Cu<sub>2</sub>O has been observed on Cu(111) and Cu(100) in the potential range between  $-0.2$  V and  $-0.02$  V vs. SHE by ECAFM.<sup>26</sup> Combined electrochemical and surface enhanced Raman experiments in the alkaline NaClO<sub>4</sub> electrolyte (pH 13) have shown the sequential formation of Cu<sub>2</sub>O followed by mixed Cu<sub>2</sub>O/Cu(OH)<sub>2</sub> layers. These species were identified by the appearance of vibrational modes at 625, 525 and 460 cm<sup>-1</sup>.<sup>34</sup> Chloride adsorption leads to interesting structural features as well as dynamics on Cu(110) at potentials negative of the oxidation potential, as studied by STM and reflection anisotropy spectroscopy.<sup>35</sup> Different methods detecting changes in alkanethiol probe molecules have enabled an analysis of copper oxide structural dynamics under conditions of atmospheric corrosion.<sup>36,37</sup> Overall, the importance of *in situ* observation for such films has been established.<sup>38</sup>

A recent review compares the knowledge of optical and electronic properties of Cu<sub>2</sub>O, Cu<sub>4</sub>O<sub>3</sub> and CuO, including a discussion of thin films prepared by different techniques.<sup>19</sup> That work also contains a thorough discussion of absorption and photoluminescence (PL) spectra, which serves as a basis for spectral interpretation here. Currently, strong computational efforts are being made to understand the band structure, defect levels and optical properties of the different oxides.<sup>16,39-46</sup> A recent comparison of structural stability and the electronic band structure of all three copper oxide compounds showed that Cu<sub>2</sub>O has a direct band gap while CuO and Cu<sub>4</sub>O<sub>3</sub> both have indirect band gaps.<sup>47</sup> Other calculations suggested Cu<sub>4</sub>O<sub>3</sub> to be metallic.<sup>19</sup>

The complex interplay between electrochemistry, the electronic structure of forming oxide films, and its effect on corrosion processes is still much less understood. This work focuses on *in situ* spectroscopic investigations of the oxide forming in different stages of the oxidation of copper, with the aim of understanding the nature of the forming oxide. For this purpose, *in situ* and *operando* spectroscopic ellipsometry and Raman spectroscopy have been carried out in alkaline solutions. The PL background observed in the Raman spectra yields additional information about the oxides. An extension of a previous analysis scheme for spectroscopic ellipsometry provides the possibility of obtaining spectra of the thin films without the need for modelling. While the spectroscopic ellipsometry yields global information, Raman spectroscopy, which has been carried out in a confocal Raman microscope, yields local information. Finally, global chemical composition of the sample surfaces was investigated *ex situ* after removal from electrochemical cells using X-ray photoelectron spectroscopy (XPS) analysing both photoelectron and Auger peaks.

## 2 Materials and methods

### 2.1 Sample preparation

Evaporated copper was used as a working electrode. Si(100) (Siegert Wafer, Aachen, Germany) single crystal wafers were

cleaned with neutral detergent Extran (VWR) and isopropanol. On the freshly cleaned surface, a 10 nm chromium adhesion layer was initially deposited. Subsequently, copper was evaporated by electron beam evaporation. Chromium and copper pellets with purity 99.999% (Wieland Edelmetalle, Pforzheim, Germany) were used. All evaporation was carried out in a Leybold Univex 450 chamber. During evaporation, the pressure was around  $6 \times 10^{-7}$  mbar. Copper was evaporated at an evaporation rate of 10 nm min<sup>-1</sup>. Typically, a layer with a thickness of 200 nm was obtained.

### 2.2 *In situ* Raman spectroscopy

*In situ* (Stokes) Raman spectra were recorded using a Labram confocal Raman microscope (Horiba Jobin Yvon, France). An objective with magnification 10 $\times$ , a numerical aperture of 0.25, was used to illuminate the sample with light from the 632 nm (1.96 eV) line of a HeNe laser, leading to an illuminated spot with  $\sim 10$   $\mu\text{m}$  diameter. Backscattered light was collected *via* the same objective and analysed on a CCD detector. Electrochemical experiments were conducted using a custom-made three electrode electrochemical cell, which was equipped with a quartz window through which the laser beam was incident on the copper surface. Electrode potential  $E$  was controlled by a Compactstat potentiostat (Ivium Technologies, Eindhoven, The Netherlands) and (unless noted otherwise) is reported here with reference to Ag|AgCl|3 M KCl. Currents are always normalised to electrode areas and reported as current density  $j$ . All experiments were conducted in 0.1 M NaOH (pH  $\approx 13$ ). The working electrode area in the cell was  $\approx 1.15$  cm<sup>-2</sup>. An Ag|AgCl|3 M KCl microreference electrode (DriRef-2SH, World Precision Instruments, Sarasota, FL, USA) was used as a reference electrode. Its electrode potential has been determined as +0.208 mV vs. standard hydrogen electrode using a calibrated Ag|AgCl|3 M KCl electrode (Metrohm, Filderstadt, Germany). A graphite rod served as a counter electrode. The electric contact of the sample was made *via* a Cu tape connecting the evaporated copper to the potentiostat. The electrolyte was not purged with inert gas, and was stagnant during the experiments.

### 2.3 Electrochemical spectroscopic ellipsometry

**2.3.1 Measurements.** Most electrochemical experimental conditions were the same as described in Section 2.2. Spectroscopic ellipsometry experiments were performed using an SE 800 spectroscopic ellipsometer (Sentech Instruments, Krailling/Berlin, Germany) and a Compactstat potentiostat (Ivium Technologies, Eindhoven, The Netherlands). The wavelength range for spectroscopic ellipsometry was 300–810 nm (1.53–4.13 eV), and the angle of incidence was 70°. The light source was a xenon lamp. A freshly prepared Cu sample was directly mounted in the optical-electrochemical cell, which was equipped with liquid flow connections, a Pt mesh counter electrode and an Ag|AgCl|3 M KCl microreference electrode (DriRef-2SH, World Precision Instruments, Sarasota, FL, USA). The working electrode area was 2.5 cm<sup>2</sup>, illuminated area on the working electrode  $\approx 0.7$  cm<sup>2</sup>. Cell design was discussed in detail elsewhere.<sup>48,49</sup> To remove oxygen, the 0.1 M NaOH electrolyte was externally saturated with argon, and purged with a rate of 2 mL min<sup>-1</sup>

for  $\approx 10$  min using a peristaltic pump (Ismatec IDEX Health and Science, Glattbrugg, Switzerland). During the measurement, the pump rate was reduced to  $10.6 \mu\text{L min}^{-1}$ . The first five ellipsometric measurements were conducted at the open circuit potential (OCP). A potential of  $-1.0$  V was subsequently applied for a certain time to reduce any oxide on the surface and to start ellipsometric experiments with an oxide-free surface. The experiments then proceeded in potentiostatic steps to more and more positive potentials. Ellipsometric measurements were carried out during these experiments. In this work, the duration of a single ellipsometric measurement was  $\approx 15$  s. The external purging with argon and the electrolyte flow through the cell at a low rate were the only differences under experimental conditions compared to the Raman experiments discussed in Section 2.2. In experiments in an electrochemical cell, the presence of oxygen had no effect on the oxide formation peaks in polarisation curves. To rule out any effect of oxygen reduction on the measurement of the reference state in ellipsometric experiments, the purging was considered appropriate. As such a reference state measurement is not used in Raman data analysis, external purging was not carried out in such experiments.

**2.3.2 Ellipsometric data analysis.** Spectra were measured of the ellipsometric parameters  $\Psi$  and  $\Delta$ , and were used to calculate the ellipsometric ratio  $\rho$

$$\rho = \frac{r_p}{r_s} = \tan(\Psi) e^{i\Delta} \quad (1)$$

of the amplitude reflection coefficients  $r_p$  and  $r_s$  for p- and s-polarised light, respectively,<sup>50,51</sup> where  $i = \sqrt{-1}$ . Data analysis was performed based on a perturbation approach as described by Lekner,<sup>51</sup> in extension to the approach discussed previously.<sup>48</sup> For layers with a total thickness  $d$  small compared to the wavelength  $\lambda$ ,  $\rho$  is expanded to first order around  $\rho_0$  for a step profile in the dielectric function, yielding<sup>51</sup>

$$\rho = \rho_0 - F J_1, \quad (2)$$

where the factor  $F$  contains details of the optical system.<sup>48,51</sup> For a system ambient—single layer—substrate, the first-order perturbation parameter  $J_1$  is given as<sup>51</sup>

$$J_1 = \frac{(\varepsilon_1 - \varepsilon_s)(\varepsilon_s - \varepsilon_2)}{\varepsilon_s} d = \left( \varepsilon_1 + \varepsilon_2 - \frac{\varepsilon_1 \varepsilon_2}{\varepsilon_s} - \varepsilon_s \right) d, \quad (3)$$

where index 1 on  $\varepsilon$  indicates the incidence medium (electrolyte), index 2 the exit medium (copper substrate) and index s the layer. The dielectric function is  $\varepsilon = (n + ik)^2$ , the square of the complex refractive index with real part  $n$  and imaginary part  $k$ . All  $\varepsilon$  and consequently also  $J_1$  depend on  $\lambda$ .

Data analysis proceeded via (1) the determination of  $\varepsilon_2(\lambda)$  from measurements of the oxide-free surface, (2) the determination of  $d$  at each electrode potential to (3) the determination of  $\varepsilon_s(\lambda)$ , i.e. the spectrum of the formed layer, as follows. First, the substrate (pseudo)dielectric function  $\varepsilon_2(\lambda)$  was determined from measurements of  $\rho_0$  according to<sup>50</sup>

$$\varepsilon_2(\lambda) = \varepsilon_1(\lambda) \left\{ \sin^2 \theta_1 + \sin^2 \theta_1 \tan^2 \theta_1 \left[ \frac{1 - \rho_0(\lambda)}{1 + \rho_0(\lambda)} \right]^2 \right\}, \quad (4)$$

with  $\theta_1$  as an angle of incidence at  $-1.0$  V where no oxide was present on the surface. The  $\lambda$ -dependence of  $\varepsilon_1$  was calculated based on literature values for the  $\lambda$ -dependence of the refractive index of water, with a correction for the concentration dependence  $dn/dc$  at a single wavelength of the electrolyte  $0.1 \text{ M NaOH}$ .<sup>52</sup> Resulting curves for  $\varepsilon_2(\lambda)$  agree with literature values within the limits of disagreement between different sources at wavelengths below  $600 \text{ nm}$ .<sup>53,54</sup> Variations in  $\varepsilon_1$  within typical deviations lead only to variations in  $\varepsilon_2(\lambda)$  lower than the difference between different literature sources.<sup>53,54</sup>

Second, at each electrode potential other than the oxide-free reference potential of  $-1.0$  V, the layer thickness  $d$  of the formed oxide layer was determined. To determine  $d$ , two different approaches have been evaluated, without differences in the final conclusions. Approach (a) uses the shift in  $\Delta$  with increasing  $d$  and is equivalent to the approach described before.<sup>55</sup> For both  $\text{CuO}$  and  $\text{Cu}_2\text{O}$  layers of thicknesses of up to  $50 \text{ nm}$ , expected ellipsometric spectra have been simulated. The  $\Delta$  values at  $\lambda = 700 \text{ nm}$  have been plotted against  $d$  and fit to a second order polynomial. The resulting calibration curve agrees to within 5% for the two oxides. Values for  $\text{Cu}_2\text{O}$  have been used to determine  $d$  from the observed difference in  $\Delta$  to the initial  $\Delta$  at the oxide-free surface. Approach (b) follows the assumption that at wavelengths  $> 650 \text{ nm}$ , the formed oxide layer is non-absorbing, i.e.  $\text{Im}(\varepsilon_s) = 0$ .<sup>48</sup> In this case, one can exploit the fact that for metallic substrates,  $\text{Im}(\varepsilon_2) \neq 0$ , hence eqn (3) can be separated into the real and imaginary part as

$$\text{Re}(J_1) = \left[ \varepsilon_1 + \text{Re}(\varepsilon_2) - \varepsilon_s - \frac{\varepsilon_1}{\varepsilon_s} \text{Re}(\varepsilon_2) \right] d, \quad (5)$$

and

$$\text{Im}(J_1) = \left[ 1 - \frac{\varepsilon_1}{\varepsilon_s} \text{Im}(\varepsilon_2) \right] d \quad (6)$$

where the  $\lambda$ -dependence was dropped. Eqn (5) and (6) form a system of equations with two unknowns  $\varepsilon_s$  and  $d$ , which can be solved to yield<sup>48</sup>

$$\varepsilon_s = \text{Re}(\varepsilon_2) - \text{Im}(\varepsilon_2) \cdot \frac{\text{Re}(J_1)}{\text{Im}(J_1)}, \quad (7)$$

and the obvious solution for  $d$  after substituting the result into eqn (5) and (6). Averaging results for all wavelengths from  $650 \text{ nm}$  to  $820 \text{ nm}$  yielded statistically relevant results for  $d$ , together with a standard deviation used as an error estimate.

Third, the data for  $\varepsilon_2(\lambda)$  and  $d$  are substituted into eqn (3), and this equation is solved numerically for  $\varepsilon_s$  at all wavelengths using the fsolve function from GNU Octave (<https://www.gnu.org/software/octave/>). Resulting solutions have been put back into eqn (3) to check if the solutions are valid. The two different approaches to determine the layer thickness yield similar spectra of  $\varepsilon_s(\lambda)$ , with numerical differences but with the same spectral features. The thicknesses obtained using approach (a) are 10–20% lower. Here, the results from approach (b) are presented, because this approach does not rely on external optical constant data. Data at higher wavelengths are not analysed in the spectra to avoid overinterpretation of the data in this wavelength range.

**2.3.3 At-a-glance visualisation of ellipsometric spectra.** On a metal surface, qualitative information can directly be obtained from an analysis of the  $\Psi$  spectra without detailed analysis. Because of the surface selection rule,<sup>56</sup> the absorption of light from a thin film strongly affects  $|r_p|$ , but leaves  $|r_s|$  almost unaffected.<sup>49,57</sup> For a more intuitive interpretation of ellipsometric spectra, the authors would like to introduce a “pseudo reflectance absorbance”, PRA, defined in analogy to reflectance absorbance, RA =  $-\log_{10}(I/I_0) = -\log_{10}(R/R_0)$ , which is commonly used to analyse reflectance spectra.<sup>56</sup> Here,  $I$  denoted the irradiance (intensity) of light at the detector, and  $R$  is the reflectivity,  $R = |r|^2$ , which strongly depends on the polarisation of light. The index 0 indicates the measurement of a reference state of the surface, in this work the oxide-free surface at negative electrode potentials.

Considering that  $|r_s| \approx |r_{s,0}|$  because of the surface selection rule implies that

$$\frac{\tan \Psi}{\tan \Psi_0} \approx \frac{|r_p|}{|r_{p,0}|}. \quad (8)$$

Consequently,

$$\text{PRA} = -\log_{10}\left(\frac{\tan^2 \Psi}{\tan^2 \Psi_0}\right) \quad (9)$$

is a useful quantity to plot for a qualitative analysis of a spectrum, as PRA  $\approx$  RA in p-polarisation.

Notice that this is not replacing a full analysis of ellipsometric data; however, using the PRA enables a visualisation of the essential feature from an absorption spectrum of a thin film on a metal surface directly from ellipsometric spectra, which will be shown for the copper system in Section 3.4. A more detailed analysis of the polarisation of reflected light also implies that averaging from an inhomogeneous sample is important, so that several  $\Psi$  exist,<sup>58,59</sup> leading to a more involved situation.

#### 2.4 Ex situ PL spectroscopy

PL spectroscopy was carried out *ex situ* after electrochemical experiments in an alpha 300 M (Witec, Ulm, Germany) confocal Raman microscope with excitation at 532 nm (2.33 eV). (No *in situ* Raman experiments conducted using this setup are shown here, because of the dominating luminescence in these spectra.)

#### 2.5 XPS

XPS (Quantera II, Physical Electronics, Chanhassen, MN, USA) was performed to investigate the chemical composition of the sample surface after electrochemical experiments. The monochromatic Al K $\alpha$  X-ray source (1486.6 eV) was operated at a pass energy of 55 eV, a step size of 0.1 eV at a measurement area of 100  $\mu\text{m} \times 100 \mu\text{m}$ . The take-off angle was 45°. The binding energy scale was referenced to the C-C signal at 284.8 eV. The quantitative analysis was carried out with CasaXPS 2.3.15 (<http://www.casaxps.com/>). Depth profiles were obtained by sputtering with an argon plasma at a voltage of 1 kV with 7 mA for the first step and then at 2 kV with a current of 7 mA for the rest of the sputter

steps. The sputtered area was 2 mm × 2 mm. The sputtering rate in copper was determined by sputtering through a 200 nm evaporated copper on a silicon wafer as 2.87 nm min<sup>-1</sup> for 1 kV and 5.77 nm min<sup>-1</sup> for 2 kV.

## 3 Results and discussion

### 3.1 Electrochemistry of copper

The cyclic voltammogram (CV) of copper in the ellipsometric *in situ* cell (Fig. 1) compares favourably with CVs from the literature.<sup>27,28,34,60</sup> The measurements in the potential region from −1.4 to 0.9 V encompassed two anodic peaks ( $A_1$  and  $A_2$ ) and the accompanying cathodic features ( $C_2$  and  $C_1$ ).  $A_1$  and  $A_2$  are typically assigned to oxidation peaks corresponding to the formation of copper(i) and copper(ii) oxides, respectively, and the related  $C_2$  and  $C_1$  reduction peaks correspond to their reduction.<sup>27,28,34,60</sup> In the ellipsometric cell, the  $C_2$  is split, which is not observed in control experiments in a bare electrochemical cell, and is also not observed in the literature. At potentials below −1.2 V, the hydrogen evolution reaction (HER) is observed. At potentials above +0.6 V, copper dissolution and the oxygen evolution reaction (OER) lead to rising current.<sup>4</sup> This behaviour is characteristic of transpassive dissolution.<sup>4</sup> The disadvantage of CV experiments is that time-dependent and potential-dependent features are interleaved. Therefore, the growth of oxide on copper was investigated with potential steps between constant electrode potentials.

### 3.2 Thickness of the oxide

Fig. 2 shows the current response and layer thickness for a sample in electrochemical potentiostatic step experiments. Before the application of a controlled potential, five ellipsometric measurements were conducted at open circuit potential (OCP). The sample was then reduced at −1.0 V for 5 min, and subsequently oxidized at −0.1, +0.1, +0.2, +0.3, +0.4 and +0.5 V, *i.e.* at potentials where no gas evolution (OER, HER) is observed, for 15 min each. During the initial reduction step at −1.0 V, the native oxide initially present on the copper surface is reduced. Subsequent application of

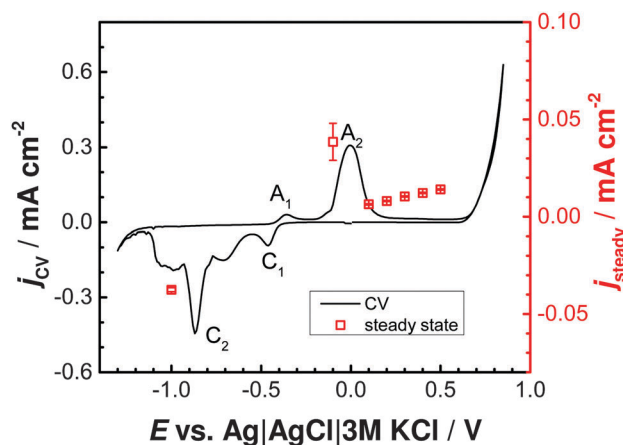
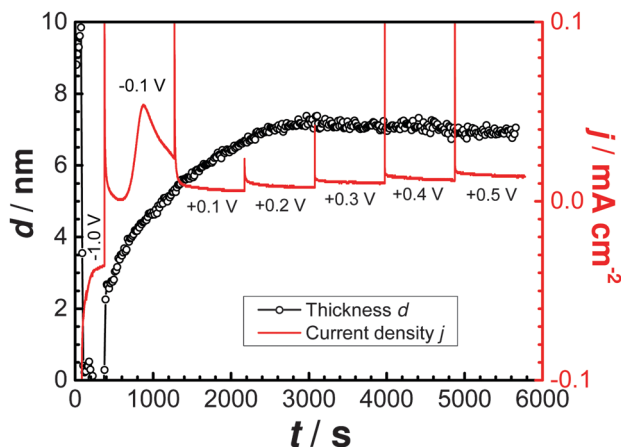


Fig. 1 CV of evaporated copper in 0.1 M NaOH in the cell used for ellipsometric experiments at a scan rate of 2 mV s<sup>-1</sup>. □ Steady-state current densities  $j_{\text{steady}}$  from the potentiostatic step experiments shown in Fig. 2.



**Fig. 2** Current densities  $j$  and thickness of the interfacial layer  $d$  as a function of experiment time  $t$ . The applied electrode potentials are indicated in the curve; the spikes in current density mark the switching of the electrode potential. Standard deviation for the thickness is on average 1.7 nm, individual error bars are omitted for clarity.

different positive potentials leads to an electrochemical oxidation. Fig. 2 shows the typical spike in current density after switching the electrode potential to  $-0.1$  V. Simultaneously, the thickness of the oxide film increases to 2 nm. While holding the potential at  $-0.1$  V, an increase in current is observed after  $\approx 200$  s at this potential. The onset of this current peak agrees with a further increase observed in the layer thickness. For all further potential jumps, the typical anodic current spikes are observed that include the capacitive current. However, the layer thickness growth at higher potentials does not have an obvious connection to the applied electrode potential. Above a potential of  $+0.3$  V, the thickness remains constant at 7 nm.

For the second half of the period at each potential as shown in Fig. 2,  $j$  was averaged to yield  $j_{\text{steady}}$ , which is overlayed with the CV in Fig. 1. At  $-0.1$  V, the result would not correspond to a steady state current density, however, at the higher potentials, this procedure yields steady state current densities. The resulting curve does not follow the CV. Integrating the currents and determining the charge assuming that only  $\text{Cu}_2\text{O}$  is formed<sup>30</sup> leads to a final thickness of  $\sim 30$  nm, which is an indication that metal dissolution is still taking place.

Because  $d$  does not increase at the last three potential steps, the current transient spikes after the potential jumps were integrated to yield a charge density  $Q$ , which in turn was used to determine a differential capacitance  $C_d = dQ/dE$ . For the last three potential jumps,  $C_d = (0.47 \pm 0.05) \text{ mF cm}^{-2}$ . Potential independence confirms the constant thickness found in ellipsometric results. The comparably large value of  $C_d$  points to the presence of a pseudocapacitance, *e.g.* from a system which can easily change its valency during polarisation.<sup>4</sup>

### 3.3 Nature of the oxides as determined by Raman spectroscopy

*In situ* Raman spectroscopy has been conducted to complement ellipsometric information with vibrational fingerprints of the

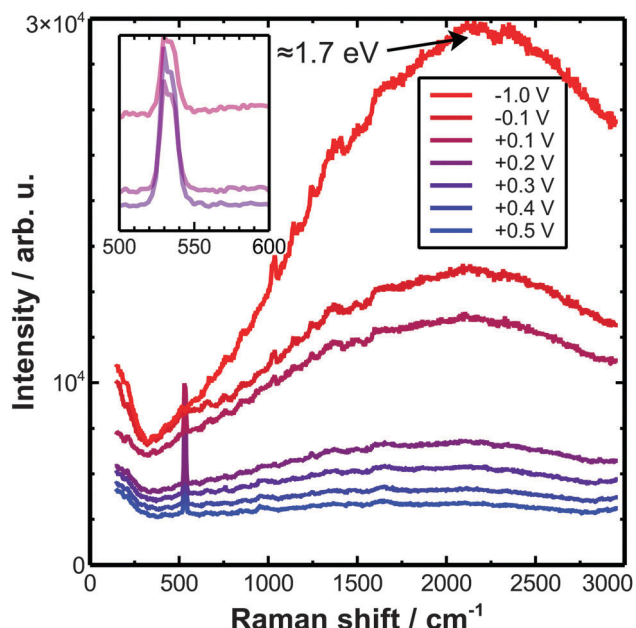


**Fig. 3** Potential-dependent Raman spectra (excitation: 633 nm; 1.96 eV) for the oxidation of copper in 0.1 M NaOH in potentiostatic steps between potentials as indicated in the graph. Spectra shown were recorded at the end of the 30 min hold period at each potential.

formed oxides. The time at which the sample was polarised at a certain potential was doubled from the ellipsometric measurements, but the potential sequence was the same as in Section 3.2. Spectra recorded at different potentials at the end of the 30 min hold period are displayed without any baseline treatment in Fig. 3. Several full time series at each potential are available in ESI† Fig. S2–S19.

Two dominant features are obvious in the spectra. There is a strong luminescence background starting from  $-1.0$  V, which decreases with increasing electrode potential. A sharp Raman feature with the maximum at  $\approx 530 \text{ cm}^{-1}$  can clearly be distinguished for the first time at  $+0.1$  V. This peak has a shoulder at higher wavenumbers centred at  $535 \text{ cm}^{-1}$ . The peak consists of two components already at its first appearance, and the lower wavenumber side becomes slightly more pronounced at higher potentials.

To assign the observed peak to a vibrational mode, it is useful to compare the results with the copper oxide vibrational spectra reported in the literature. Both bulk  $\text{CuO}$  and  $\text{Cu}_2\text{O}$  exhibit a major Raman feature at  $\approx 635 \text{ cm}^{-1}$ , whereas  $\text{Cu}(\text{OH})_2$  shows a band at  $490 \text{ cm}^{-1}$ .<sup>33,34</sup> None of these features is prominently observed here. On the other hand, the Raman spectrum of  $\text{Cu}_4\text{O}_3$  is dominated by an  $A_{1g}$  mode at  $\approx 540 \text{ cm}^{-1}$ .<sup>21,61</sup> The spectra here hence show the presence of  $\text{Cu}_4\text{O}_3$  in the oxide films starting at  $+0.1$  V. Two possible explanations may be put forward for the split nature of the peak observed here. First, the spectrum of  $\text{Cu}_4\text{O}_3$  contains an  $E_g$  mode at slightly lower wavenumbers. Second,  $\text{Cu}_2\text{O}$  shows peaks around this wavenumber, too.<sup>61–63</sup> In the wavenumber region investigated here,  $\text{Cu}_2\text{O}$  shows the sharpest peak at  $\approx 210 \text{ cm}^{-1}$ .<sup>21,62,63</sup> Indeed, in some spectra a small peak is observed there. The presence of  $\text{Cu}_2\text{O}$  can therefore not be

excluded. On the other hand, the Raman spectrum of CuO is dominated by an  $A_g$  mode at  $\approx 300 \text{ cm}^{-1}$ , which was only observed once in a single experiment at +0.3 V.

More details emerge when analysing the time dependence of the spectra at one electrode potential from different series of experiments, which are displayed in the ESI.<sup>†</sup> To understand the behaviour of the spectra shown there, one needs to keep in mind that Raman spectroscopy carried out in a confocal microscope as in this work is a local probe, probing an area of a few 10  $\mu\text{m}$  in diameter. On the other hand, the measured current and also the ellipsometric experiments discussed here probe extended areas of the surface. In two of the three experimental series shown here, the peak at  $\approx 530 \text{ cm}^{-1}$  attributed to Cu<sub>4</sub>O<sub>3</sub> is first observed at +0.1 V, while in the third experiment it is already observed at -0.1 V. The first appearance of the peak does not correlate with the potential jumps, but at some apparently random time at a certain potential. Such a behaviour is not surprising when inspecting the layer thickness growth shown in Fig. 2, which happens also during holding the electrode potential constant. The sudden appearance of the peak is consistent with a nucleation phenomenon. As soon as Cu<sub>4</sub>O<sub>3</sub> crystals nucleated in the illuminated spot, the peak is visible, and remains almost unaffected in subsequent experiments. The peak may also disappear again after its initial formation [series 2, Fig. S11; series 3, Fig. S17 (ESI<sup>†</sup>)]. After disappearance, in series 3 it reappeared at the next potential (ESI<sup>†</sup> Fig. S18). Disappearance and reappearance show no obvious relation to the electrode potential. In the period between disappearance and reappearance of the peak, two very broad peaks are detected centred around 590  $\text{cm}^{-1}$  and 470  $\text{cm}^{-1}$  (ESI<sup>†</sup> Fig. S17 and S18), attributed to strongly disordered or even amorphous species. As Cu(OH)<sub>2</sub> shows a peak at 490  $\text{cm}^{-1}$ <sup>33,34</sup> hydroxide may be involved here. The observed changes are a sign of the constant remodelling of the interfacial film, through which current flows that may induce amorphisation of the film, with loss in the sharp Raman peaks which would indicate a crystalline structure.

The time dependent spectra also show further, less prominent peaks. (In addition, spectra also show the water deformation mode  $\approx 1645 \text{ cm}^{-1}$ <sup>64</sup> and the third series show a peak at  $\approx 1080 \text{ cm}^{-1}$  attributed to the symmetric C–O stretching mode of carbonate,<sup>65–67</sup> which is known to accumulate in alkaline solutions. These two are not of interest in this work.) The intensity of a peak at  $\approx 960 \text{ cm}^{-1}$  correlates with the intensity of the main peak at 530  $\text{cm}^{-1}$ , which is why it is attributed to the second order 2A<sub>1g</sub> mode of the same. Most importantly, a peak at  $\approx 705 \text{ cm}^{-1}$  is observed in the transient stage before the occurrence of the peak at 530  $\text{cm}^{-1}$ , mostly at -0.1 V. This peak is not observed in any known copper oxide,<sup>19,21,34,61–63,68</sup> which makes a certain assignment impossible. As this peak is clearly originating from a transient structure which appears before the formation of crystalline Cu<sub>4</sub>O<sub>3</sub>, it may be related to a structure containing Cu<sup>II</sup> ions on a “wrong” lattice site, *e.g.* on Cu<sup>I</sup> sites. However, many alternatives can be imagined, including a metastable Cu<sub>4</sub>O<sub>3</sub> precursor. A Cu<sub>2</sub>O-like precursor oxide was reported as detected by fast transient measurements.<sup>69</sup>

### 3.4 Electronic structure *via* absorption and photoluminescence spectroscopy

Especially the initial spectra shown in Fig. 3 show a strong photoluminescence centred at  $\approx 1.7 \text{ eV}$ , even with a fine structure. This luminescence disappears at higher electrode potentials. Looking at the data from time series 1 (ESI<sup>†</sup> Fig. S2–S7) shows that this luminescence strongly decreases in intensity as soon as the Raman peak at  $\approx 530 \text{ cm}^{-1}$  appears. This decrease in intensity with beginning of the observation of the Raman peak of crystalline Cu<sub>4</sub>O<sub>3</sub> points to defects as the origin of this luminescence, as opposed to a band to band transition in one of the involved materials. A candidate for this observed luminescence involves copper vacancies (V<sub>Cu</sub>), as their thermodynamic energy level has been calculated to be  $\approx 1.6 \text{ eV}$  below the conduction band.<sup>41</sup> In the experimental literature, peaks associated with several defects have been reported in the PL spectrum of Cu<sub>2</sub>O, with doubly charged oxygen vacancies (V<sub>O</sub><sup>2+</sup>) around 1.7 eV.<sup>16,19</sup> The observed fine structure may be related to the electric field.<sup>70</sup> It is rather remarkable that strong PL is already observed in the spectra recorded at -1.0 V. At this potential, the peak cannot originate from a bulk-like oxide, but rather may be caused from the disordered first monolayer of OH/O adsorbed to the copper surface at these potentials. The presence of hydroxide at these potentials was proposed in a recent electrochemical work.<sup>71</sup> This observation also reminds us that in the reference state used for ellipsometric data analysis (Section 2.3.2), the interface is not as ideal as assumed.

Further insight into the oxide's electronic structure may be obtained from the analysis of the absorption spectrum obtained as a result of the analysis of ellipsometric spectra. Fig. 4a shows the PRA spectra (Section 2.3.3) recorded during oxidation. Spectra show a peak at  $\approx 2.1 \text{ eV}$ , and a very broad feature peaking slightly below 3.5 eV, with a shoulder at higher photon energies. There are only minor differences between the different electrode potentials. However, the features in the spectra become more developed with higher electrode potentials, which is consistent with the slow growth observed. Analysing the first two spectra at -0.1 V shows that the shape of the second spectrum already closely matches the shape of the further spectra. Only the peak at 3.5 eV is still not developed.

Only the very first spectrum recorded immediately after the electrode potential jump is significantly different. A very small peak at 2.0 eV, *i.e.* slightly shifted compared to its later position, is visible. At photon energies  $> 3 \text{ eV}$ , no feature is yet developed. Consequently, the structure responsible for the peak at lower photon energies develops before the entity leading to the absorption at 3.5 eV.

Results from the full analysis of ellipsometric data (see Section 2.3.2) are shown in Fig. 5a. These spectra look qualitatively similar to the PRA spectra shown in Fig. 4. There is a sharp band at  $\approx 2.2 \text{ eV}$ , and a broad band centred at  $\approx 3.3 \text{ eV}$ . Spectra show only minor changes between the different potentials, with the spectrum obtained at potentials above 0 V showing slightly more developed features. For comparison, the PL spectrum

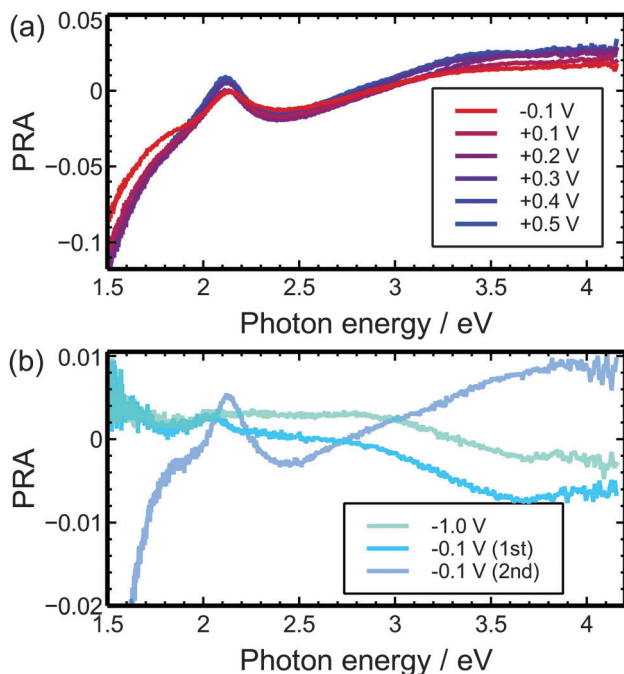


**Fig. 4** Pseudo-reflectance absorbance (PRA) spectra obtained from the ellipsometric  $\Psi$  spectra as defined in eqn (9). (a) Spectra obtained at the end of the hold period at the potential as indicated. (b) Spectra of the initial phase of oxidation. The last spectrum recorded at the reference potential  $-1.0\text{ V}$  and the first two spectra at the potential  $-0.1\text{ V}$  where oxide formation is observed are shown.

recorded *ex situ* with  $2.33\text{ eV}$  excitation after finalising the experiment is shown in Fig. 5b, which also shows a peak at  $\approx 2.2\text{ eV}$ .

When comparing the spectra obtained here *in situ* to those obtained for different copper oxides,<sup>19,72,73</sup> one notices that the spectra obtained here are completely different from those of pure copper oxides. The oxide layers obtained here must therefore contain several different components. Understanding the spectra of copper oxides is overall rather involved. Computations of the dielectric function of  $\text{Cu}_2\text{O}$  have shown that for certain maxima in the spectra, many different transitions contribute,<sup>46</sup> *e.g.* because of electron–hole interactions. A similar situation may occur in the other oxides.

For an interpretation of the spectra, the PL is a good starting point. Strong PL is also observed *in situ* when exciting with  $532\text{ nm}/2.33\text{ eV}$ . The current state of knowledge is that there is no PL from  $\text{CuO}$ .<sup>19</sup> If  $\text{Cu}_4\text{O}_3$  has an indirect band gap,<sup>47</sup> no strong PL is expected—the same holds also if it is metallic.<sup>19</sup> The observation of PL is therefore a strong indication of the presence of  $\text{Cu}_2\text{O}$ . The good agreement between PL and the absorption spectrum (*via*  $k$ ) makes it likely that the same fundamental process is responsible for both.  $\text{Cu}_2\text{O}$  has four transitions, known as yellow, green, blue and indigo lines.<sup>19,61</sup> The one lowest in energy at  $2.17\text{ eV}$  (“yellow”) corresponds to the forbidden direct band to band transition.<sup>19</sup> Here, we attribute the observed peaks in PL and  $k$  to this transition. Defects in the  $\text{Cu}_2\text{O}$  lattice break the symmetry and hence typically relax the transition rules. Here, we attribute the

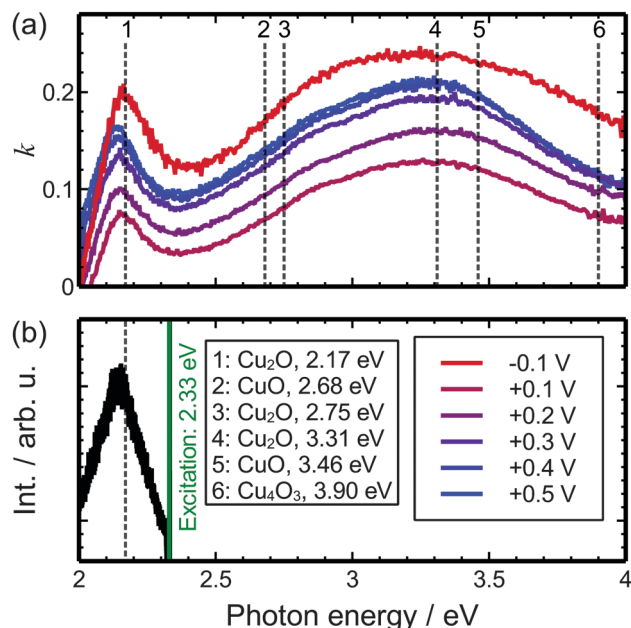


**Fig. 5** (a) Imaginary part  $k$  of refractive index of the growing oxide layer on copper determined as described in Section 2.3.2 at the potentials indicated in (b). Spectra recorded at the end of the hold time at the respective potential are shown. The vertical lines show selected important transitions experimentally found for  $\text{Cu}_2\text{O}$ ,  $\text{Cu}_4\text{O}_3$  and  $\text{CuO}$ ,<sup>19</sup> also labelled in (b). (b) *Ex situ* PL spectrum of the electrochemically oxidized sample, excited with  $532\text{ nm}$  ( $2.33\text{ eV}$ ). Energy scale applies to both subfigures.

observation of the otherwise inactive transition to the prominent presence of defects in the films.

The strongest feature in the  $\text{Cu}_2\text{O}$  absorption spectrum is expected to be at  $3.31\text{ eV}$ ,<sup>19</sup> which is close to the maximum of the peak observed here. For  $\text{CuO}$ , the strongest peak is at  $3.46\text{ eV}$ ,<sup>19</sup> already on the decreasing side of the  $k$  spectrum observed here. Like in the Raman spectra (Section 3.3),  $\text{CuO}$  can be ruled out as dominating the spectra. The  $\text{Cu}_4\text{O}_3$  spectrum is dominated by a peak at  $3.9\text{ eV}$ , which is a region in which differences are observed— $k$  decreases towards higher wavenumbers. Overall, defect-rich films may have significantly different absorption spectra compared to those with little defects.<sup>57</sup>

### 3.5 Surface analysis

Fig. 6 shows the sputtering profiles obtained by XPS after electrochemical experiments, which gives more insight into the chemical composition of the oxide layers.

The surface spectrum shows a strong satellite peak in the  $\text{Cu}$  2p spectrum indicative of  $\text{Cu}^{\text{II}}$ .<sup>74–78</sup> The position of the peak in the  $\text{Cu}$  LMM spectrum ( $917.8\text{ eV}$ ) also confirms the presence of  $\text{Cu}^{\text{II}}$ . This may be the consequence of the oxidation of the substrate after coming into contact with air. Peak fitting of the  $\text{Cu}$  2p<sub>3/2</sub> region yielded a ratio  $\text{Cu}^{\text{I}}:\text{Cu}^{\text{II}}$  of  $\approx 2:1$ . After the initial sputtering step of  $3\text{ nm}$ , the strong satellite peak disappears and a weak satellite peak can be observed in the  $\text{Cu}$  2p spectrum, which matches the one exhibited by  $\text{Cu}^{\text{I}}$ . The  $\text{Cu}$  LMM peak position ( $916.8\text{ eV}$ ) also confirms that below the surface, significant amounts of  $\text{Cu}^{\text{I}}$  are present.<sup>74–77</sup>

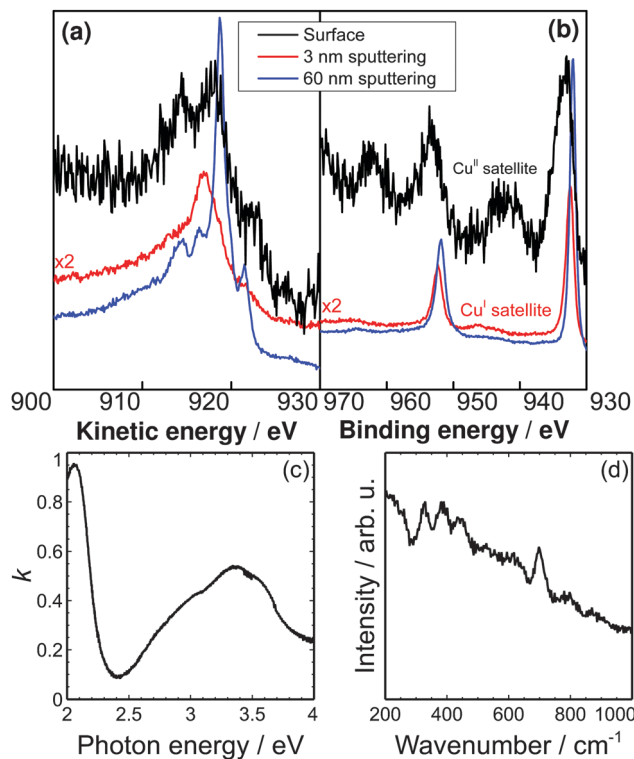


**Fig. 6** *Ex situ* analysis of the layer after electrochemical *in situ* spectroscopic ellipsometry experiments. (a) Auger LMM spectra and (b) Cu 2p spectra obtained during XPS sputter depth profiling. Sputter depths are indicated in the graph. (c)  $k$  spectrum. (d) Raman spectrum after excitation with 633 nm (1.96 eV).

Quantification of the Cu 2p<sub>3/2</sub> region yields a ratio Cu<sup>I</sup>:Cu<sup>II</sup> of  $\approx 9:1$ . However, it is known that sputtering may reduce Cu<sup>II</sup> to Cu<sup>I</sup>.<sup>75,79</sup> Further, Cu<sup>I</sup> is hard to quantify in the presence of Cu<sup>0</sup>.<sup>78</sup> Longer sputtering, up to 60 nm into the metal, resulted in complete removal of the oxide. Both the Cu 2p and Cu LMM spectra show peaks indicative of copper metal.<sup>74–77</sup> Overall, XPS confirms the presence of both oxidation states of copper. Results do not contradict the presence of Cu<sub>4</sub>O<sub>3</sub>, nor do they confirm it.

To connect these results to the results from *in situ* measurements, *ex situ* ellipsometric and Raman spectra are shown in Fig. 6c and d. Spectra of  $k$  are very similar in shape to those recorded *in situ* (Fig. 5), with a slight shift of the initial maximum to lower wavenumbers, and different peak heights. The qualitative similarities lead to the conclusion that the dominating electronic transitions are preserved. On the other hand, the Raman spectrum is qualitatively different from the spectra *in situ* (Fig. 3). Here, peaks at  $\approx 325\text{ cm}^{-1}$ , and  $\approx 380\text{ cm}^{-1}$  may be attributed to slightly shifted A<sub>g</sub> and B<sub>g</sub> modes of CuO.<sup>21</sup> The peak at  $\approx 440\text{ cm}^{-1}$  may be the Raman-inactive A<sub>u</sub> mode,<sup>21</sup> which becomes active because of a relaxation of transition rules due to defects. The highest mode at  $\approx 695\text{ cm}^{-1}$  is in a region where no mode of copper oxides is typically observed.<sup>19,21</sup> Importantly, the peak at  $532\text{ cm}^{-1}$ , which dominates the *in situ* spectra and was attributed to Cu<sub>4</sub>O<sub>3</sub>, was absent in the *ex situ* spectra.

## 4 Summary and conclusions

The passive layer on copper is more complex than the view of a duplex layer presented so far in the literature. While during growth at high temperatures, the presence of an inner layer of Cu<sub>2</sub>O and an outer layer of CuO has been observed,<sup>7</sup> the Raman results for the electrochemical passive films obtained here lead to the conclusion that the mixed oxide, Cu<sub>4</sub>O<sub>3</sub>, must play a prominent role in the film. The large interfacial (pseudo)capacitance obtained for the films also indicates the presence of a structure in which the ions can easily change their valency, supporting the presence of Cu<sub>4</sub>O<sub>3</sub>. Upon removal from the electrolyte, Cu<sub>4</sub>O<sub>3</sub> transforms into CuO, and presumably to the classical duplex layer. Raman spectra indicate that in solution both crystalline as well as amorphous regions are present in the film. PL spectra show the presence of Cu<sub>2</sub>O *via* its normally inactive “yellow” line at 2.17 eV. Excitation below the band gap at 1.96 eV leads to strong defect-related luminescence, presumably also of a Cu<sub>2</sub>O-like structure. The obtained absorption spectra in the energy range 2–4 eV cannot be explained with a simple superposition of the spectra of Cu<sub>2</sub>O and CuO, as expected for a duplex layer. Also, the inclusion of Cu<sub>4</sub>O<sub>3</sub> does not change this disagreement. The conclusion is therefore that defects also play a prominent role in these passive films, and lead to significantly altered absorption spectra. Overall, the films are strongly dynamic, and transformations between amorphous and crystalline regions occur. The amount of evidence for the presence of CuO *in situ* is extremely limited. On the other hand, the Raman spectra point to the formation of CuO after removal from solution. Fig. 7 visualizes schematically the view of copper oxides presented in this work.

The properties of the passive films are only weakly dependent on the electrode potential. After the films start to grow at  $-0.1\text{ V}$  the growth in thickness does not correlate with potential jumps. This observation is in disagreement with the point defect model.<sup>80</sup> Above  $+0.3\text{ V}$ , the film thickness remains constant despite potential changes. Also, the absorption spectra do not

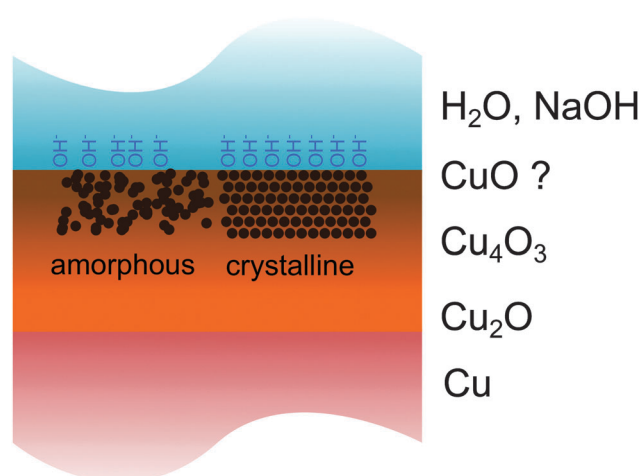


**Fig. 7** Schematic summary of the structural picture of the passive films on copper in NaOH obtained in this study.

change their shape except in the initial phase of the oxide formation, indicating only gradual changes in the electronic structure. Evidence for a precursor oxide in the initial stages of the film formation is found, which shows a Raman peak at  $705\text{ cm}^{-1}$ . Overall, the passive film on copper may have more similarities to the passive film on iron than originally perceived. On iron, a concentration gradient in  $\text{Fe}^{2+}$  and  $\text{Fe}^{3+}$  on the lattice of  $\text{Fe}_3\text{O}_4/\text{Fe}_2\text{O}_3$  is present.<sup>4</sup> Because of the difference in the crystal structure between the copper oxides,<sup>19</sup> a directly analogous situation is not possible. However, a gradient in composition of  $\text{Cu}^+$  and  $\text{Cu}^{2+}$  is still likely.

The evidence presented here relies mostly on the interpretation of vibrational and electronic spectra. We note here that there is already disagreement between some of these reference spectra.<sup>19,21</sup> This is likely caused by the non-stoichiometry of the present compounds. Reference data are needed for oxides grown at a controlled oxygen partial pressure, but to the knowledge of the authors are not available. With currently available reference data it is also hard to distinguish  $\text{Cu}_4\text{O}_3$  from a mixture of  $\text{Cu}_2\text{O}$  and  $\text{CuO}$  by XPS. Likewise, efforts of the computational side, including computation of the full spectra of the respective oxides,<sup>46</sup> are needed for a full understanding of the chemistry at the copper/solution interface.

The results presented here are the outcome of a fundamental study. In practise, these results imply that the oxides forming on copper as a result of high temperature oxidation and of aqueous oxidation are different. For often inhibitor-based corrosion protection of copper-based alloys in aqueous solutions, the implication is that when choosing inhibitors, their interaction – including the electronic interaction and possible electron transfer – with the  $\text{Cu}_4\text{O}_3$  may be important.

## Acknowledgements

C.T. acknowledges a scholarship from the International Max Planck Research School for Surface and Interface Engineering in Advanced Materials (IMPRS-SurMat). A.S. acknowledges funding from the Max Planck Society in the frame of MaxNet Energy. The authors thank Prof. M. Stratmann for continuous support as well as Andreas D. Wieck and Stefan M. Wippermann for helpful discussions.

## References

- European Copper Institute, accessed October 2015, <http://www.copperalliance.eu/>.
- M. Miodownik, *Stuff Matters: The Strange Stories of the Marvellous Materials that Shape Our Man-made World*, Penguin, London, UK, 2014.
- C. Gattinoni and A. Michaelides, *Surf. Sci. Rep.*, 2015, **70**, 424–447.
- H. Kaesche, *Corrosion of Metals: Physicochemical Principles and Current Problems*, Springer, Berlin, Germany, 2003.
- K. Mimura, J.-W. Lim, M. Isshiki, Y. Zhu and Q. Jiang, *Metall. Mater. Trans. A*, 2006, **37**, 1231–1237.
- I. Platzman, R. Brener, H. Haick and R. Tannenbaum, *J. Phys. Chem. C*, 2008, **112**, 1101–1108.
- J.-W. Lim, J. Iijima, Y. Zhu, J. H. Yoo, G.-S. Choi, K. Mimura and M. Isshiki, *Thin Solid Films*, 2008, **516**, 4040–4046.
- P. Keil, R. Frahm and D. Lützenkirchen-Hecht, *Corros. Sci.*, 2010, **52**, 1305–1316.
- N. de Zoubov, C. Vanleuvenhaghe and M. Pourbaix, in *Atlas of electrochemical equilibria in aqueous solutions*, ed. M. Pourbaix, National Association of Corrosion Engineers/Centre Belge d'Etude de la Corrosion CEBELCOR, Houston/Bruxelles, 1974, ch. 14.1, pp. 384–392.
- M. Wei, N. Braddon, D. Zhi, P. A. Midgley, S. K. Chen, M. G. Blamire and J. L. MacManus-Driscoll, *Appl. Phys. Lett.*, 2005, **86**, 072514.
- M. Sieberer, J. Redinger and P. Mohn, *Phys. Rev. B: Condens. Matter Mater. Phys.*, 2007, **75**, 035203.
- A. Bhaumik, A. M. Shearin, R. Patel and K. Ghosh, *Phys. Chem. Chem. Phys.*, 2014, **16**, 11054–11066.
- Y. Shen, M. Guo, X. Xia and G. Shao, *Acta Mater.*, 2015, **85**, 122–131.
- K. Akimoto, S. Ishizuka, M. Yanagita, Y. Nawa, G. K. Paul and T. Sakurai, *Sol. Energy*, 2006, **80**, 715–722.
- O. Messaoudi, H. Makhlof, A. Souissi, I. Ben assaker, M. karyaoui, A. Bardaoui, M. Oueslati and R. Chtourou, *J. Alloys Compd.*, 2014, **611**, 142–148.
- J.-W. Park, H. Jang, S. Kim, S.-H. Choi, H. Lee, J. Kang and S.-H. Wei, *J. Appl. Phys.*, 2011, **110**, 103503.
- H. Yu, J. Yu, S. Liu and S. Mann, *Chem. Mater.*, 2007, **19**, 4327–4334.
- F. Marabelli, G. B. Parravicini and F. Salghetti-Drioli, *Phys. Rev. B: Condens. Matter Mater. Phys.*, 1995, **52**, 1433–1436.
- B. K. Meyer, A. Polity, D. Reppin, M. Becker, P. Hering, P. J. Klar, T. Sander, C. Reindl, J. Benz, M. Eickhoff, C. Heiliger, M. Heinemann, J. Bläsing, A. Krost, S. Shokovets, C. Müller and C. Ronning, *Phys. Status Solidi B*, 2012, **249**, 1487–1509.
- S. Nikitine, J. Grun and M. Sieskind, *J. Phys. Chem. Solids*, 1961, **17**, 292–300.
- L. Debbichi, M. C. Marco de Lucas, J. F. Pierson and P. Krüger, *J. Phys. Chem. C*, 2012, **116**, 10232–10237.
- J. P. Hu, D. J. Payne, R. G. Egddell, P.-A. Glans, T. Learmonth, K. E. Smith, J. Guo and N. M. Harrison, *Phys. Rev. B: Condens. Matter Mater. Phys.*, 2008, **77**, 155115.
- C. Wang, Y. Wang, X. Liu, F. Diao, L. Yuan and G. Zhou, *Phys. Chem. Chem. Phys.*, 2014, **16**, 17487–17492.
- M. M. Islam, B. Diawara, V. Maurice and P. Marcus, *J. Mol. Struct.*, 2009, **903**, 41–48.
- A. Martínez-Ruiz, M. G. Moreno and N. Takeuchi, *Solid State Sci.*, 2003, **5**, 291–295.
- N. Ikemiya, T. Kubo and S. Hara, *Surf. Sci.*, 1995, **323**, 81–90.
- V. Maurice, H.-H. Strehblow and P. Marcus, *J. Electrochem. Soc.*, 1999, **146**, 524–530.
- V. Maurice, H. H. Strehblow and P. Marcus, *Surf. Sci.*, 2000, **458**, 185–194.
- V. Maurice, L. H. Klein, H.-H. Strehblow and P. Marcus, *J. Electrochem. Soc.*, 2003, **150**, B316–B324.

- 30 E. Martinez-Lombardia, V. Maurice, L. Lapeire, I. De Graeve, K. Verbeken, L. Kestens, P. Marcus and H. Terryn, *J. Phys. Chem. C*, 2014, **118**, 25421–25428.
- 31 J. Kunze, V. Maurice, L. H. Klein, H.-H. Strehblow and P. Marcus, *J. Phys. Chem. B*, 2001, **105**, 4263–4269.
- 32 J. Kunze, V. Maurice, L. H. Klein, H.-H. Strehblow and P. Marcus, *Corros. Sci.*, 2004, **46**, 245–264.
- 33 J. C. Hamilton, J. C. Farmer and R. J. Anderson, *J. Electrochem. Soc.*, 1986, **133**, 739–745.
- 34 H. Y. H. Chan, C. G. Takoudis and M. J. Weaver, *J. Phys. Chem. B*, 1999, **103**, 357–365.
- 35 G. Barati, V. Solokha, K. Wandelt, K. Hingerl and C. Cobet, *Langmuir*, 2014, **30**, 14486–14493.
- 36 M. Schwind, S. Hosseinpour, C. M. Johnson, C. Langhammer, I. Zorić, C. Leygraf and B. Kasemo, *Langmuir*, 2013, **29**, 7151–7161.
- 37 S. Hosseinpour, M. Schwind, B. Kasemo, C. Leygraf and C. M. Johnson, *J. Phys. Chem. C*, 2012, **116**, 24549–24557.
- 38 I. Díez-Pérez, F. Sanz and P. Gorostiza, *Curr. Opin. Solid State Mater. Sci.*, 2006, **10**, 144–152.
- 39 R. Laskowski, P. Blaha and K. Schwarz, *Phys. Rev. B: Condens. Matter Mater. Phys.*, 2003, **67**, 075102.
- 40 M. Nolan and S. D. Elliott, *Phys. Chem. Chem. Phys.*, 2006, **8**, 5350–5358.
- 41 D. O. Scanlon, B. J. Morgan, G. W. Watson and A. Walsh, *Phys. Rev. Lett.*, 2009, **103**, 096405.
- 42 D. O. Scanlon, B. J. Morgan and G. W. Watson, *J. Chem. Phys.*, 2009, **131**, 124703.
- 43 D. Wu, Q. Zhang and M. Tao, *Phys. Rev. B: Condens. Matter Mater. Phys.*, 2006, **73**, 235206.
- 44 A. Önsten, M. Måansson, T. Claesson, T. Muro, T. Matsushita, T. Nakamura, T. Kinoshita, U. O. Karlsson and O. Tjernberg, *Phys. Rev. B: Condens. Matter Mater. Phys.*, 2007, **76**, 115127.
- 45 J. P. Hu, D. J. Payne, R. G. Eggell, P.-A. Glans, T. Learmonth, K. E. Smith, J. Guo and N. M. Harrison, *Phys. Rev. B: Condens. Matter Mater. Phys.*, 2008, **77**, 155115.
- 46 F. Bruneval, N. Vast, L. Reining, M. Izquierdo, F. Sirotti and N. Barrett, *Phys. Rev. Lett.*, 2006, **97**, 267601.
- 47 M. Heinemann, B. Eifert and C. Heiliger, *Phys. Rev. B: Condens. Matter Mater. Phys.*, 2013, **87**, 115111.
- 48 Y. Chen and A. Erbe, *Surf. Sci.*, 2013, **607**, 39–46.
- 49 Y. Chen, P. Schneider and A. Erbe, *Phys. Status Solidi A*, 2012, **209**, 846–853.
- 50 R. M. A. Azzam and N. M. Bashara, *Ellipsometry and Polarized Light*, Elsevier Science, Amsterdam, The Netherlands, 1999.
- 51 J. Lekner, *Theory of Reflection of Electromagnetic and Particle Waves*, Springer, Dordrecht, Netherlands, 1987.
- 52 *Handbook of Chemistry and Physics*, ed. W. M. Haynes, CRC Press, Boca Raton, 94th edn, 2012.
- 53 S. Babar and J. H. Weaver, *Appl. Opt.*, 2015, **54**, 477–481.
- 54 A. D. Rakic, A. B. Djurišić, J. M. Elazar and M. L. Majewski, *Appl. Opt.*, 1998, **37**, 5271–5283.
- 55 M. Hans, A. Erbe, S. Mathews, Y. Chen, M. Solioz and F. Mücklich, *Langmuir*, 2013, **29**, 16160–16166.
- 56 A. Erbe, A. Sarfraz, C. Toparli, K. Schwenzfeier and F. Niu, Optical absorption spectroscopy at interfaces, in *Soft matter at aqueous interfaces*, ed. P. Lang and Y. Liu, Springer, Cham, Switzerland, 2016, vol. 917, DOI: 10.1007/978-3-319-24502-7\_14.
- 57 Y. Chen, P. Schneider, B.-J. Liu, S. Borodin, B. Ren and A. Erbe, *Phys. Chem. Chem. Phys.*, 2013, **15**, 9812–9822.
- 58 R. Sigel and A. Erbe, *Appl. Opt.*, 2008, **47**, 2161–2170.
- 59 A. Erbe, K. Tauer and R. Sigel, *Langmuir*, 2009, **25**, 2703–2710.
- 60 J. Kunze, V. Maurice, L. H. Klein, H.-H. Strehblow and P. Marcus, *Electrochim. Acta*, 2003, **48**, 1157–1167.
- 61 Y. Petroff, P. Y. Yu and Y. R. Shen, *Phys. Rev. B: Solid State*, 1975, **12**, 2488–2495.
- 62 V. A. Maroni, Characterization: Raman Spectroscopy Measurements and Interpretations, in *High Temperature Superconductors*, ed. R. Bhattacharya and M. P. Panthanaman, Wiley-VCH, Weinheim, Germany, 2010, pp. 67–92.
- 63 M. Ivanda, D. Waasmaier, A. Endriss, J. Ihringer, A. Kirfel and W. Kiefer, *J. Raman Spectrosc.*, 1997, **28**, 487–493.
- 64 G. E. Walrafen and R. T. W. Douglas, *J. Chem. Phys.*, 2006, **124**, 114504.
- 65 M. Prencipe, F. Pascale, C. M. Zicovich-Wilson, V. R. Saunders, R. Orlando and R. Dovesi, *Phys. Chem. Miner.*, 2004, **31**, 559–564.
- 66 L. Valenzano, F. J. Torres, K. Doll, F. Pascale, C. M. Zicovich-Wilson and R. Dovesi, *Z. Phys. Chem.*, 2006, **220**, 893–912.
- 67 E. E. Coleyshaw, G. Crump and W. P. Griffith, *Spectrochim. Acta, Part A*, 2003, **59**, 2231–2239.
- 68 X. K. Chen, J. C. Irwin and J. P. Franck, *Phys. Rev. B: Condens. Matter Mater. Phys.*, 1995, **52**, R13130.
- 69 M. Lohrengel, J. Schultze, H. Speckmann and H.-H. Strehblow, *Electrochim. Acta*, 1987, **32**, 733–742.
- 70 J. Deiss, A. Daunois and S. Nikitine, *Solid State Commun.*, 1969, **7**, 1417–1419.
- 71 D. Starovetsky, N. Sezin, E. Abelev, T. Cohen-Hyams and Y. Ein-Eli, *J. Electrochem. Soc.*, 2014, **161**, C77–C82.
- 72 T. Ito, T. Kawashima, H. Yamaguchi, T. Masumi and S. Adachi, *J. Phys. Soc. Jpn.*, 1998, **67**, 2125–2131.
- 73 C. Malerba, F. Biccari, C. Leonor Azanza Ricardo, M. D'Incau, P. Scardi and A. Mittiga, *Sol. Energy Mater. Sol. Cells*, 2011, **95**, 2848–2854.
- 74 T. Fleisch and G. Mains, *Appl. Surf. Sci.*, 1982, **10**, 51–62.
- 75 G. Panzner, B. Egert and H. Schmidt, *Surf. Sci.*, 1985, **151**, 400–408.
- 76 K. J. Blobaum, D. Van Heerden, A. J. Wagner, D. H. Fairbrother and T. P. Weihs, *J. Mater. Res.*, 2003, **18**, 1535–1542.
- 77 R. Benoit, Y. Durand, B. Narjoux and G. Quintana, 2015, <http://www.lasurface.com/>.
- 78 XPS Knowledge Base, August 2015, <http://xpssimplified.com/elements/copper.php>.
- 79 D. Frost, A. Ishitani and C. McDowell, *Mol. Phys.*, 1972, **24**, 861–877.
- 80 C. Y. Chao, L. F. Lin and D. D. Macdonald, *J. Electrochem. Soc.*, 1981, **128**, 1187–1194.